Journal of Rock Mechanics and Geotechnical Engineering 14 (2022) 169–179

Contents lists available at ScienceDirect

Journal of Rock Mechanics and Geotechnical Engineering

journal homepage: www.jrmge.cn

Full Length Article

Numerical analysis of slope collapse using SPH and the SIMSAND critical state model

Zhao Lu [a,b], Zhuang Jin [c,d,e,*], Panagiotis Kotronis [f]

[a] Civil and Environmental Engineering, University of Macau, Macau, China
[b] Research and Development Center, Shenzhen Foundation Engineering Co. Ltd., Shenzhen, 518000, China
[c] Department of Civil and Environmental Engineering, The Hong Kong Polytechnic University, Hong Kong, China
[d] Southern Marine Science and Engineering Guangdong Laboratory (Guangzhou), Guangzhou, 510000, China
[e] Department of Ocean Science and Engineering, Southern University of Science and Technology, Shenzhen, 518000, China
[f] Institut de Recherche en Génie Civil et Mécanique (GeM), École Centrale de Nantes, Université de Nantes, Rue de la Noë, Nantes, 44321, France

ARTICLE INFO

Article history:
Received 21 December 2020
Received in revised form
20 February 2021
Accepted 31 March 2021
Available online 1 May 2021

Keywords:
Granular material
Smoothed particle hydrodynamics (SPH)
Large deformations
Landslide
Critical state
Slope failure
Sand

ABSTRACT

Geological disasters such as slope failure and landslides can cause loss of life and property. Therefore, reproducing their evolution process is of great importance for risk assessment and mitigation. The recently developed SIMSAND critical state sand model combined with the smoothed particle hydrodynamics (SPH) method is adopted in this work to study slope failure under large deformations. To illustrate the efficiency and accuracy of the SIMSAND-SPH approach, a series of slope collapse studies using the discrete element method (DEM) considering various particle shapes (i.e. spherical, tetrahedral and elongated) is adopted as benchmarks. The parameters of the SIMSAND model are calibrated using DEM triaxial tests. In comparison to the DEM simulations, the runout distance and final slope height are well characterized with the SIMSAND-SPH approach with less computational cost. All comparisons show that the SIMSAND-SPH approach is highly efficient and accurate, which can be an alternative numerical tool to simulate real scale granular flow.

1. Introduction

Geological disasters accompanied by large deformations and failure of geomaterials and geo-structures occur regularly around the world, e.g. landslides (Liu et al., 1995; Wang et al., 2021), snow avalanche/rockfalls (Bovet et al., 2010), debris flow (Jeong et al., 2015), dam breaks (Shakibaeinia and Jin, 2011), soil liquefaction (Di and Sato, 2003), seepage damage (Maeda et al., 2006; Yang et al., 2019a), tunnel excavation (Shi et al., 2019) and dynamic erosion (Yang et al., 2019b, 2020; Lei et al., 2020). Large-scale solid-failure sliding plays an important role in these geological hazards that generally cause huge destructions and present a long-distance impact. Reproducing their evolution process is therefore necessary for risk assessment and mitigation.

In recent years, the discrete element method (DEM) has been often used to numerically reproduce granular collapse (Lacaze et al., 2008; Soundararajan, 2015; Utili et al., 2015) and landslides (Barla et al., 2012; Scholtès and Donzé, 2012; Lu et al., 2014). Unlike the finite element method (FEM), DEM treats the material as an assemblage of rigid discrete particles. Contact forces are used to reproduce the particle interactions and thus the physical nature of the granular body is taken into account. It is worth noting that the number of particles in the DEM simulations should be very small. Therefore, parallel computational strategies are often necessary in order to reduce the computational cost. However, the number of particles in the majority of DEM simulations is limited for computational efficiency and often far from a realistic physical model. In view of this, coupling the DEM with other numerical methods (such as finite elements, finite differences and the material point method (MPM)) is regarded as an alternative approach. Taking the FEM-DEM coupling for example, the granular materials presenting large deformations are modeled by DEM particles, whereas finite elements are used for the domain presenting small deformations. This allows the number of DEM particles to be greatly reduced, improving the computational efficiency, so that the model can be applied to real case studies. Nevertheless, the

* Corresponding author. Department of Civil and Environmental Engineering, The Hong Kong Polytechnic University, Hong Kong, China.
E-mail address: jinzhuang2015@outlook.com (Z. Jin).

Peer review under responsibility of Institute of Rock and Soil Mechanics, Chinese Academy of Sciences.

https://doi.org/10.1016/j.jrmge.2021.03.009

computational efficiency of the DEM is relatively low compared to phenomenological constitutive models, such as the classical Mohr-Coulomb model (Coulomb, 1973) or the more advanced Modified Cam Clay model (Roscoe and Burland, 1968), the SIMSAND (simple sand) model (Yin et al., 2016; Jin et al., 2017a) and the 3D elastoplastic model (Hong et al., 2017, 2020).

Another important limitation stems from the fact that severe deformations of the mesh limit the application of the FEM. In contrast, mesh-free methods such as smooth particle hydrodynamics (SPH) and MPM are good alternatives to simulate landslides (McDougall and Hungr, 2004; Haddad et al., 2010; Cascini et al., 2014; Llano-Serna et al., 2016; Soga et al., 2016; Peng et al., 2019; Ren et al., 2019; Xiong et al., 2021). For example, SPH has been successfully adopted to analyze the impact of landslide-induced tsunami on shipping in reservoir (Wang et al., 2021). However, numerical simulations considering mesh-free methods and state-dependent advanced constitutive models are still seldom in the literature (Jin et al., 2018a; Yin et al., 2018a).

In order to efficiently reproduce slope collapse taking into account some advanced features such as the influence of soil density and large deformations, the SIMSAND critical state constitutive model and the SPH method are hereafter coupled. In order to validate the approach, DEM slope collapse simulations are used as benchmarks. For the DEM simulations, three different particle shapes are considered: spherical shape (SS), tetrahedral shape (TS) and elongated shape (ES). The SIMSAND-SPH parameters are calibrated from DEM triaxial tests using an optimization-based identification method. Comparisons of the DEM and the SIMSAND-SPH simulations illustrate the performance of the approach and its ability to take into account the effect of the particle shape and the soil density on the final deposit configuration.

2. Numerical model

2.1. Smoothed particle hydrodynamics (SPH)

The SPH method, implemented in the finite element code ABAQUS/Explicit, is adopted due to its ability to simulate large deformation problems. This method was introduced in 1977 (Gingold and Monaghan, 1977), initially for problems in astrophysics. Further developments extended SPH to solid mechanics where its main advantage is the possibility of dealing with larger local distortions over mesh-based methods.

The core of SPH is interpolation, and all macroscopic variables (such as density, pressure, speed, etc.) are conveniently expressed as integral interpolation calculations by means of a set of values at discrete points. The field variable $f(x)$ at point x in the numerical domain Ω is obtained by the following equation accounting for the effect of neighbouring particles:

$$f(x) = \int_{\Omega} f(x')W(x-x',h)\,\mathrm{d}x' \tag{1}$$

where W is a weighting function, the so-called kernel or smoothing function. Particles in the numerical domain interact with each other through the kernel function with a characteristic radius known as the “smoothing length”, represented by h in Eq. (1). In other words, the physical quantity of any particle is obtained by summing the relevant properties of all the particles that lie within the range of the kernel. The function $f(x)$ in Eq. (1) is further approximated by the summation over neighbouring particles as

$$f(x) = \sum_{i=1}^{N} f(x_i)W(x-x_i,h)V_i = \sum_{i=1}^{N} f(x_i)W(x-x_i,h)\frac{m_i}{\rho_i} \tag{2}$$

where V_i, ρ_i and m_i are the volume, density and mass of the particle i, respectively; and N is the number of influencing particles. The derivatives of the above interpolated integrals are obtained by ordinary derivation without the use of finite differences and without grids, which is the main advantage of SPH over conventional numerical methods (finite differences or finite elements).

By assigning at each particle its own smoothing length and allowing it to vary with time, a SPH simulation is automatically adapted on local conditions. In a very dense region where particles are close, the smoothing length can be relatively short, yielding a high spatial resolution. Conversely, in low density regions where individual particles are far apart and the resolution is low, the smoothing length can be increased, optimizing the computational time. Since the particles can interact and then separate during calculation, SPH is able to deal with very large deformations (Baranowski et al., 2014).

2.2. Explicit finite element method (FEM)

The SPH method implemented in ABAQUS uses the explicit time integration method (Hibbitt et al., 2014). The equilibrium condition is first written with the balance of internal and external forces:

$$\boldsymbol{M}\ddot{\boldsymbol{u}}_{(t)} = \boldsymbol{P}_{(t)} - \boldsymbol{I}_{(t)} \tag{3}$$

where $\boldsymbol{M}$ is the mass matrix, $\ddot{\boldsymbol{u}}$ is the acceleration, $\boldsymbol{P}$ is the applied external force vector, $\boldsymbol{I}$ is the internal force vector, and the subscript t refers to the time in an explicit dynamic step.

The equations of motion for the body are then integrated using the explicit time central-difference integration rule as follows:

$$\left.\begin{aligned}\dot{\boldsymbol{u}}_n &= \frac{\boldsymbol{u}_{n+1}-\boldsymbol{u}_{n-1}}{2\Delta t}\\ \ddot{\boldsymbol{u}}_n &= \frac{\boldsymbol{u}_{n+1}-2\boldsymbol{u}_n+\boldsymbol{u}_{n-1}}{(\Delta t)^2}\end{aligned}\right\} \tag{4}$$

where $\boldsymbol{u}$ is the displacement, $\dot{\boldsymbol{u}}$ is the velocity, and Δt is the time increment. For stability reasons, the time increment Δt should be smaller than a limited value, i.e. $\Delta t \approx L_{\min}/c_{\mathrm{d}}$, where $L_{\min}$ is the smallest finite element dimension and c_{d} is the dilatory wave speed. The incremental displacement is used to calculate the incremental strain. The stresses are updated using the constitutive model and then the internal forces up to a new equilibrium state.

2.3. SIMSAND, a critical state-based model for sand

The SIMSAND model is based on the classical Mohr-Coulomb model with some additional advanced features: the critical state concept (Yin et al., 2016; Jin et al., 2017a), nonlinear elasticity, nonlinear plastic hardening, interlocking effects and a simplified three-dimensional (3D) strength criterion. The model is able to capture both the state-dependent peak strength and stress-dilatancy (contraction or dilation) (Jin et al., 2017a). The basic constitutive equations are summarized in Table 1. The model parameters and their definitions are summarized in Table 2. Their calibration can be carried out using either trial-error (Wu et al., 2017) or optimization methods (Jin et al., 2016a, b, 2019a).

The SIMSAND model was implemented into ABAQUS/Explicit as a user-defined constitutive model, via the user material subroutine VUMAT. The implementation of the model follows the procedure

Table 1
Basic constitutive equations of the SIMSAND model.

Components	Constitutive equations	Note
Elasticity	$\dot{\varepsilon}^{e}_{ij} = \frac{1+\nu}{3K(1-2\nu)}\sigma'_{ij} - \frac{\nu}{3K(1-2\nu)}\sigma'_{kk}\delta_{ij}$, $K = K_0 p_{at}\frac{(2.97-e)^2}{1+e}\left(\frac{p'}{p_{at}}\right)^{\zeta}$	p_{at} is the atmospheric pressure (p_{at} = 101.3 kPa), and p' is the effective mean pressure
Yield surface	$f = \frac{q}{p'} - H$	q is the deviatoric stress
Potential surface	$\frac{\partial g}{\partial p'} = A_d\left(M_{pt} - \frac{q}{p'}\right)$, $\frac{\partial g}{\partial s_{ij}} = \{1 \quad 1 \quad 1 \quad 1 \quad 1 \quad 1\}$	M_{pt} is the stress ratio corresponding to the phase transformation
Hardening rule	$H = \frac{M_p \varepsilon^{p}_{d}}{k_p + \varepsilon^{p}_{d}}$	M_p is the peak stress ratio
Critical state with interlocking effects	$e_c = e_{ref} - \lambda\left(\frac{p'}{p_{at}}\right)^{\xi}$, $\tan\varphi_p = \left(\frac{e_c}{e}\right)^{n_p}\tan\varphi_\mu$, $\tan\varphi_{pt} = \left(\frac{e_c}{e}\right)^{-n_d}\tan\varphi_\mu$	e_c is the critical state void ratio, φ_p is the peak friction angle, φ_{pt} is the phase transformation friction angle, φ_μ is the critical state friction angle, and n_p and n_d are the interlocking parameters controlling the degree of interlocking due to neighbouring particles (Yin et al., 2010; Yin and Chang, 2013)
3D strength criterion	$M_p = \frac{6\sin\varphi_p}{3-\sin\varphi_p}\left[\frac{2c_1{}^4}{1+c_1^4+(1-c_1^4)\sin(3\theta)}\right]^{\frac{1}{4}}$, $c_1 = \frac{3-\sin\varphi_p}{3+\sin\varphi_p}$ $M_{pt} = \frac{6\sin\varphi_{pt}}{3-\sin\varphi_{pt}}\left[\frac{2c_2{}^4}{1+c_2^4+(1-c_2^4)\sin(3\theta)}\right]^{\frac{1}{4}}$, $c_2 = \frac{3-\sin\varphi_{pt}}{3+\sin\varphi_{pt}}$	θ is the Lode's angle, and its effect is introduced as proposed by Sheng et al. (2000), and Yao et al. (2004, 2008, 2009)

Table 2
Parameters of the SIMSAND model used in slope collapse simulations.

Parameter	Definition	SS	TS	ES	SS_R01
K_0	Referential bulk modulus (dimensionless)	100	100	100	100
ν	Poisson's ratio	0.2	0.2	0.2	0.2
n	Elastic constant controlling nonlinear Stiffness	0.51	0.51	0.51	0.51
φ_μ	Critical state friction angle	18.5°	24°	26°	24°
e_{ref}	Initial critical state void ratio	0.76	0.76	0.74	0.84
λ	Constant controlling the nonlinearity of CSL	0.04	0.04	0.04	0.04
ξ	Constant controlling the nonlinearity of CSL	0.3	0.3	0.3	0.3
A_d	Constant of magnitude of the stress-dilatancy	1	1	1	1
k_p	Plastic modulus related constant	0.0015	0.0015	0.0015	0.0015
n_p	Interlocking related peak strength parameter	3.3	3.3	3.3	2.3
n_d	Interlocking related phase transformation parameter	1	1	1	1

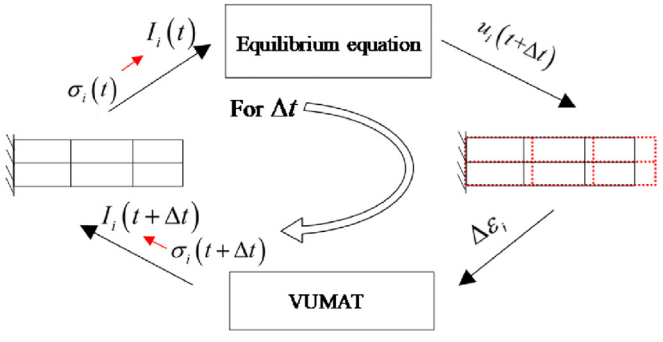

Fig. 1. Flowchart of explicit analysis of the SIMSAND model combined with the SPH method in ABAQUS/Explicit.

shown in Fig. 1 (Hibbitt et al., 2014). The cutting plane algorithm (Ortiz and Simo, 1986) is adopted for the stress integration. The implementation was verified by simulating drained triaxial tests.

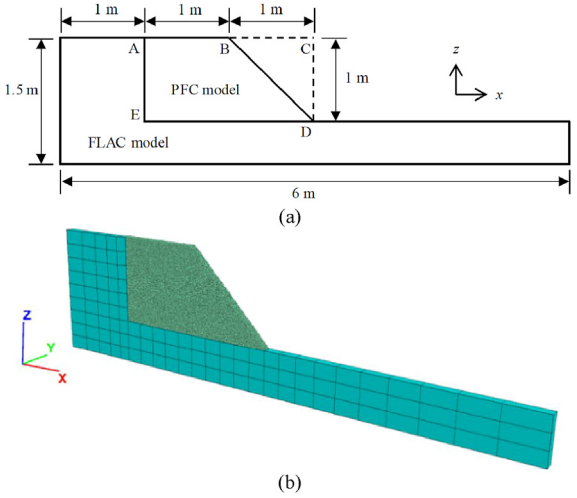

Fig. 2. Schematic plot and spatial discretisation of the slope.

3. Slope collapse simulation using discrete element method (DEM)

In order to validate the combined SIMSAND-SPH approach, a series of DEM simulations is first conducted and used as benchmark data. More specifically, the 3D discrete element software PFC^{3D} coupled with the finite difference code FLAC^{3D} are used for the simulations. Fig. 2 shows the schematic diagram and spatial discretisation of the slope that has the following dimensions: height is 1 m, top width is 2 m, bottom width is 6 m, and an angle is 45°. The slope thickness in the y direction is 0.1 m, which is about 10 times the average particle size (d_{50}). In the discrete particle region, the total number of particles is about 100,000. The slope is divided in two regions, as shown in Fig. 2: the PFC model region where discrete particles are used for the discretisation, and the FLAC model region where finite elements are used for the discretisation. The corresponding areas (PFC and FLAC areas) of the model are built to match the characteristics of slopes in the reality.

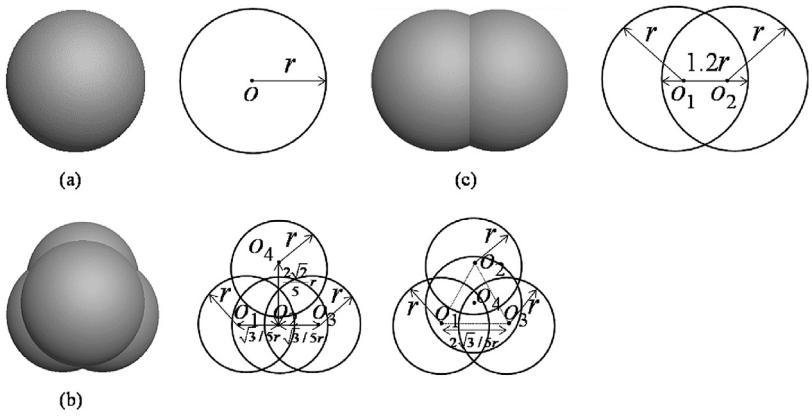

Fig. 3. Particle shapes: (a) Spherical, (b) tetrahedral, and (c) elongated.

In order to study the effect of particle shape on landslides, three kinds of particle shapes are studied: SS, TS and ES, as displayed in Fig. 3. Furthermore, a "dense" slope and a "loose" slope are considered. For the "dense" slope, the initial friction coefficient of the particles is considered equal to 0. Under the action of gravity, the particles can thus fall and deposit more easily, thereby generating a dense slope. For the "loose" slope, the initial friction coefficient of the particles is taken equal to 1. Table 3 lists the parameters of the 8 studied slope types. In the discrete particle region (PFC model), the contacts between the particles are described with a linear contact model, as shown in Table 4. In the finite volume area (FLAC model), the classical Mohr-Coulomb constitutive model is adopted, calibrated from drainage triaxial tests (Table 5). A gravity field is applied to the entire model.

Table 3
Parameters of the discrete particles for the 8 slopes.

Test No.	Particle shape	Rolling resistance	Relative density	e_0	Number of particles
1	SS	0	Dense	0.629	107,936
2	SS	0	Loose	0.736	102,277
3	TS	0	Dense	0.475	118,109
4	TS	0	Loose	0.681	104,930
5	ES	0	Dense	0.481	117,997
6	ES	0	Loose	0.672	105,871
7	SS	0.1	Dense	0.629	107,936
8	SS	0.1	Loose	0.736	102,277

Table 4
Inter-discrete particle properties.

Density, ρ_σ (kg/m^3)	Friction coefficient, μ		Normal contact stiffness, k_n (N/m)	Tangential contact stiffness k_s (N/m)
	Particle-particle	Particle-wall		
2500	0.5	0.0/0.5	1×10^7	6×10^6

Table 5
Parameters in the finite volume area.

Particle shape	Kind of slope	Young's modulus, E (kPa)	Poisson's ratio	Friction angle (°)	Dilation angle,ψ (°)	Cohesion, c (kPa)
SS	Dense	3800	0.3	24	30	0
	Loose	1300	0.3	24	13	0
TS	Dense	4300	0.3	33	31	0
	Loose	1000	0.3	33	15	0
ES	Dense	4400	0.3	36	33	0
	Loose	1100	0.3	36	17	0

Table 6
Calibrated parameters of the SIMSAND constitutive model.

Particle shape	e_{ref}	λ	ξ	φ	k_p	A_d	n_p	n_d
SS (rolling resistance = 0)	0.76	0.04	0.3	18.5	0.0015	1	3.3	1
TS	0.76	0.04	0.3	24	0.0015	1	3.3	1
ES	0.74	0.04	0.3	26	0.0015	1	3.3	1
SS (rolling resistance = 0.1)	0.84	0.04	0.3	24	0.0015	1	2.3	1

4. Slope collapse simulation using the combined SIMSAND-SPH approach

4.1. Numerical model

The geometric size of the DEM calculations is followed in the SIMSAND-SPH approach. The discrete particle and finite volume regions are now replaced by SPH particles and conventional Lagrangian finite elements, respectively. For the SPH domain, a cell size of 0.015 m is estimated by checking mesh-dependency and the total number of particles is 55,300. In the Lagrangian domain, the element size and number are consistent with those of the FLAC^{3D} model. The inner restraining wall is supposed to be smooth and the friction between particles and inner surface of restraining wall is negligible. The bottom of the slope is considered fixed while symmetrical conditions are assumed for the four lateral boundaries. In the finite element area, the classical Mohr-Coulomb constitutive model is again adopted and calibrated from drainage triaxial tests (see Table 5), while the SIMSAND model is considered in the SPH domain. A gravity field is applied to the entire model.

It is worth noting that compared to the DEM cases which require an average simulation time of 24 h for each simulation by adopting 8 CPU cores (processor clock speed equals 2.5 GHz), the average computation time for each SPH case approximately equals 2 h. Moreover, several cases can be simultaneously calculated on the TAIYI server in the Center for Computational Science and Engineering at Southern University of Science and Technology, Shenzhen, China. Therefore, the calculation efficiency of proposed method is acceptable.

4.2. Calibration of the SIMSAND model parameters

A series of DEM drained triaxial tests is conducted to calibrate the parameters of the SIMSAND constitutive model. For the three kinds of particle shapes, a total of 6 tests, i.e. 3 tests on dense samples and 3 tests on loose samples, are carried out under different confining pressures (10 kPa, 5 kPa and 2 kPa). Compared

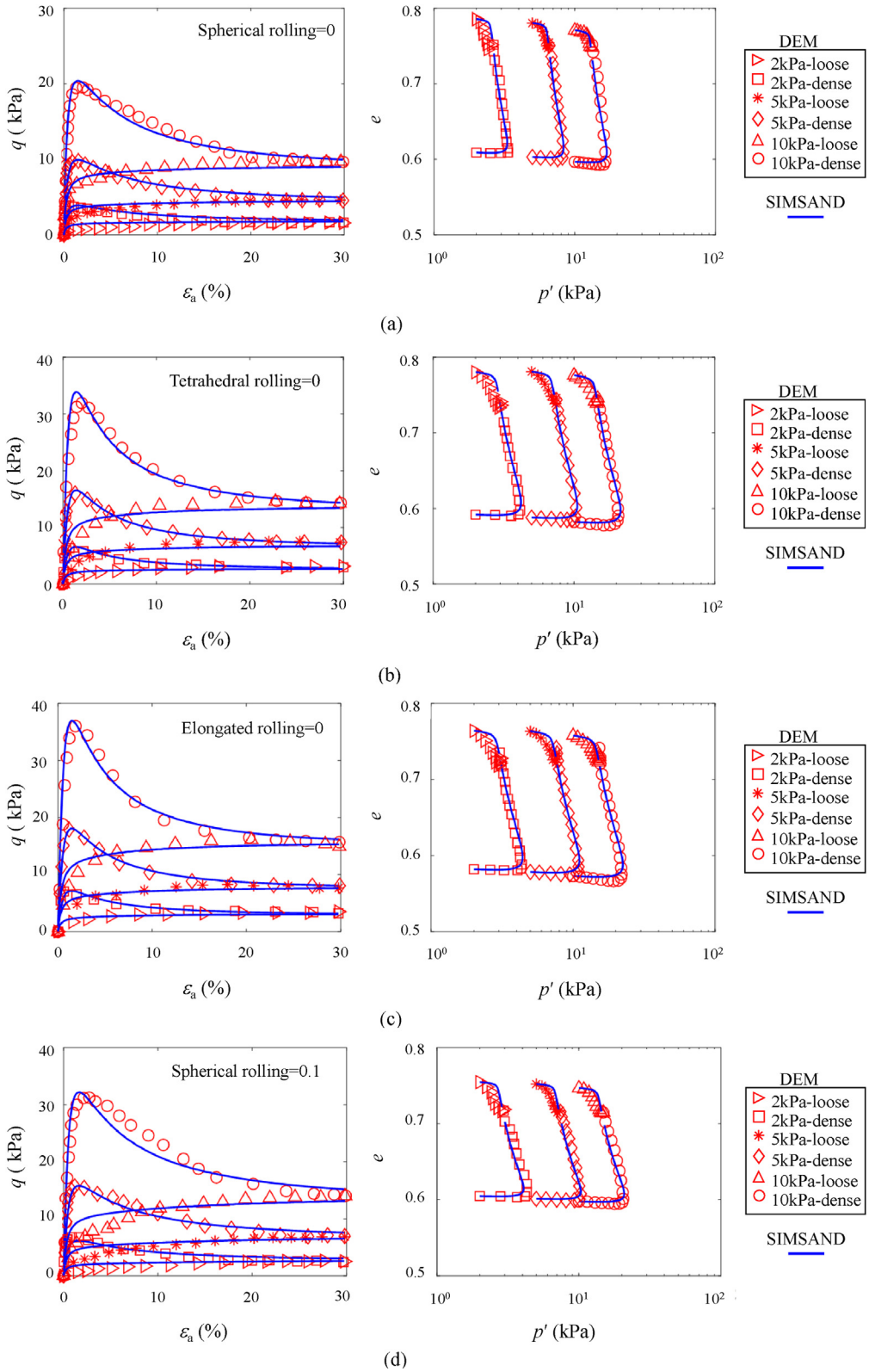

Fig. 4. Comparison between DEM triaxial tests (red symbols) and the SIMSAND constitutive model for different particle shapes (blue lines): (a) SS (rolling resistance = 0); (b) TS (rolling resistance = 0); (c) ES (rolling resistance = 0); and (d) SS (rolling resistance = 0.1).

to DEM simulation, the simulated performance of SPH significantly depends on the selected soil model and parameters. Only the appropriate soil model with optimal parameters adopted in SPH can generate the ideal simulation performance. To obtain a set of accurate parameters, the model parameters are determined through optimization-based or Bayesian-based parameter identification procedure (Jin et al., 2017b, 2018b, 2019b; Yin et al., 2017, 2018b; Jin and Yin, 2020). The parameters with more importance are put into the optimization procedure, as summarized in Table 6. An interesting phenomenon can be observed for the parameters optimized with the optimization-based or Bayesian-based parameter identification procedure. The largest difference in the model parameters is in the friction angle values, while other model parameters remain basically the same. One possible reason is that the different geometries (SS, TS and ES) lead to different contact conditions between the particles in the DEM simulation. As the particles become rough (from spherical to tetrahedral particles), the friction and shearing between the particles will increase on a microscopic level, resulting in the increase of friction angle on macroscopic level. Fig. 4 presents the results of the SIMSAND model compared with the DEM triaxial data. A good agreement is observed between both simulations.

5. Results and discussion of slope collapse simulation

During the landslide process, the top width of the slope gradually decreases and the slip particles move along the upper boundary to the foot of the slope and slide to the far end. The maximum runout particle distance is named D_m and the final top width of the slope L_f. The "loose" slope generated by spherical particles that do not consider the particle rotation effect should have the largest landslide distance. In Fig. 5, it can be seen that even in this extreme case, the maximum displacement of the FLAC and Lagrangian domains is very small (less than 1 mm), and it is therefore ignored. Only the large deformation area results, discretized with DEM or SPH, are discussed hereafter.

Figs. 6 and 7 show the final failure modes of the 8 cases using the DEM and the SPH approaches, respectively. It can be seen from Fig. 6 that the particle shape has a significant effect on landslide morphology. The cases shown in Fig. 6a and e have the largest runout distance D_m. The top of the slope is completely destroyed in the "loose" slope case (Fig. 6e). For the cases of regular tetrahedron (Fig. 6b) and elongated particles (Fig. 6c), the slope runout distances are relatively small and the final deposit configurations are similar, indicating that the mechanical properties of the two particle shapes are relatively close. For the cases shown in Fig. 6d and h, where the anti-rotation effect of the particles is considered, the runout distance D_m decreases and the top slope width L_f increases, compared with the cases presented in Fig. 6a and e. The results obtained by the SPH method (Fig. 7) show the same trends.

In order to quantify the accuracy of the simulations, the final deposit configurations provided by the DEM and SPH are presented in Fig. 8. A good agreement can be observed for different soil densities and particle shapes. The values of the runout distance D_m and the slope width L_f by SPH follow closely the DEM benchmark results.

Fig. 9 monitors the velocity field at several time steps for the 8 slopes considering different initial conditions provided by SPH. The runout distance D_m tends to be stable around $T = 3$ s for all slopes. It can be observed that the particle velocity at the foot of all slopes is zero at this time step, only a small number of particles near the top of the slope are still moving. It is also obvious that the particle shape has a significant effect on the landslide morphology. From Fig. 9a–g and for different particle shapes (i.e. SS, TS, ES), the time required for the slope collapse to reach the final stable state (i.e. when the velocity of all particles reaches zero) decreases in sequence. Furthermore, as shown in Fig. 9d and g, the rolling resistance increases the time for the collapse to reach

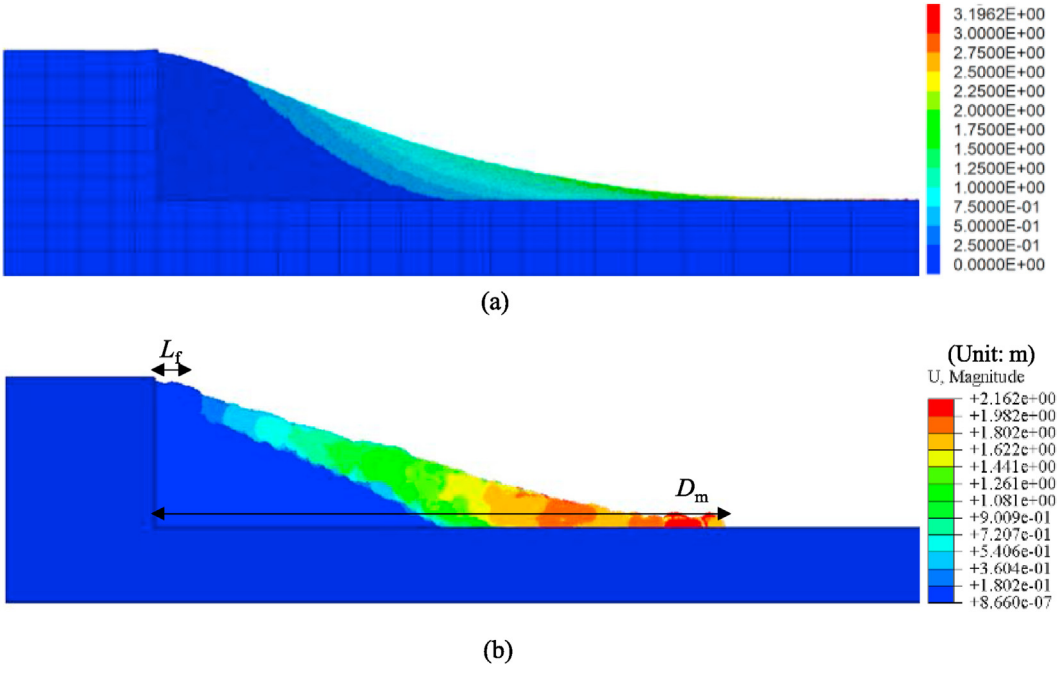

Fig. 5. Displacement field of a "loose" slope with spherical particles without rolling resistance: (a) DEM and (b) SPH.

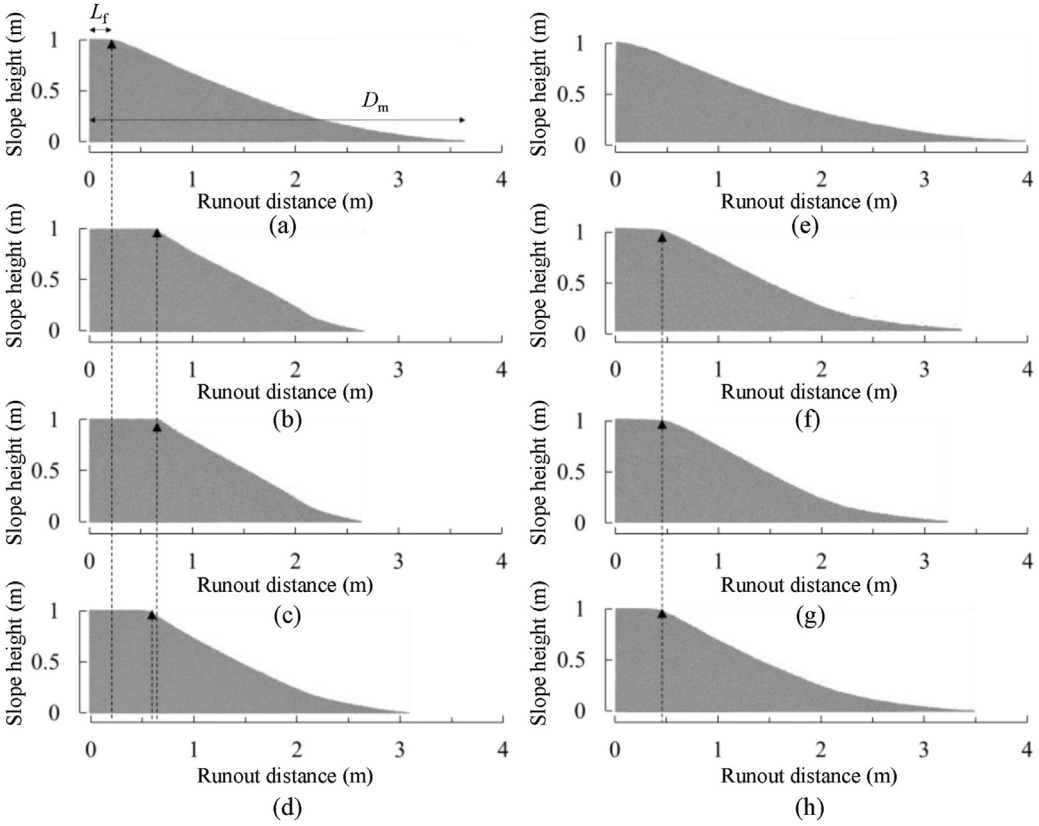

Fig. 6. Final failure patterns by DEM: (a)–(d) "Dense" slopes with (a) SS (no rolling resistance), (b) TS, (c) ES, and (d) SS (rolling resistance of 0.1); (e)–(h) "Loose" slopes with (e) SS (no rolling resistance), (f) TS, (g) ES, and (h) SS (rolling resistance of 0.1).

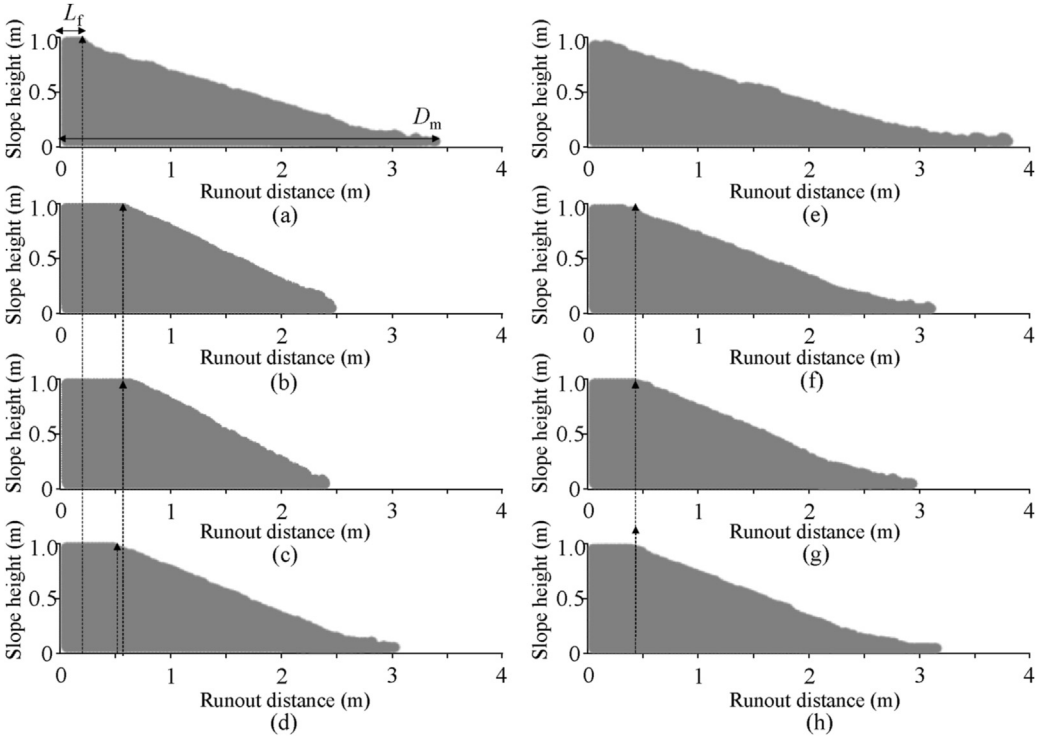

Fig. 7. Final failure patterns by SPH: (a)–(d) "Dense" slopes with (a) SS (no rolling resistance), (b) TS, (c) ES, and (d) SS (rolling resistance of 0.1); (e)–(h) "Loose" slopes with (e) SS (no rolling resistance), (f) TS, (g) ES, and (h) SS (rolling resistance of 0.1).

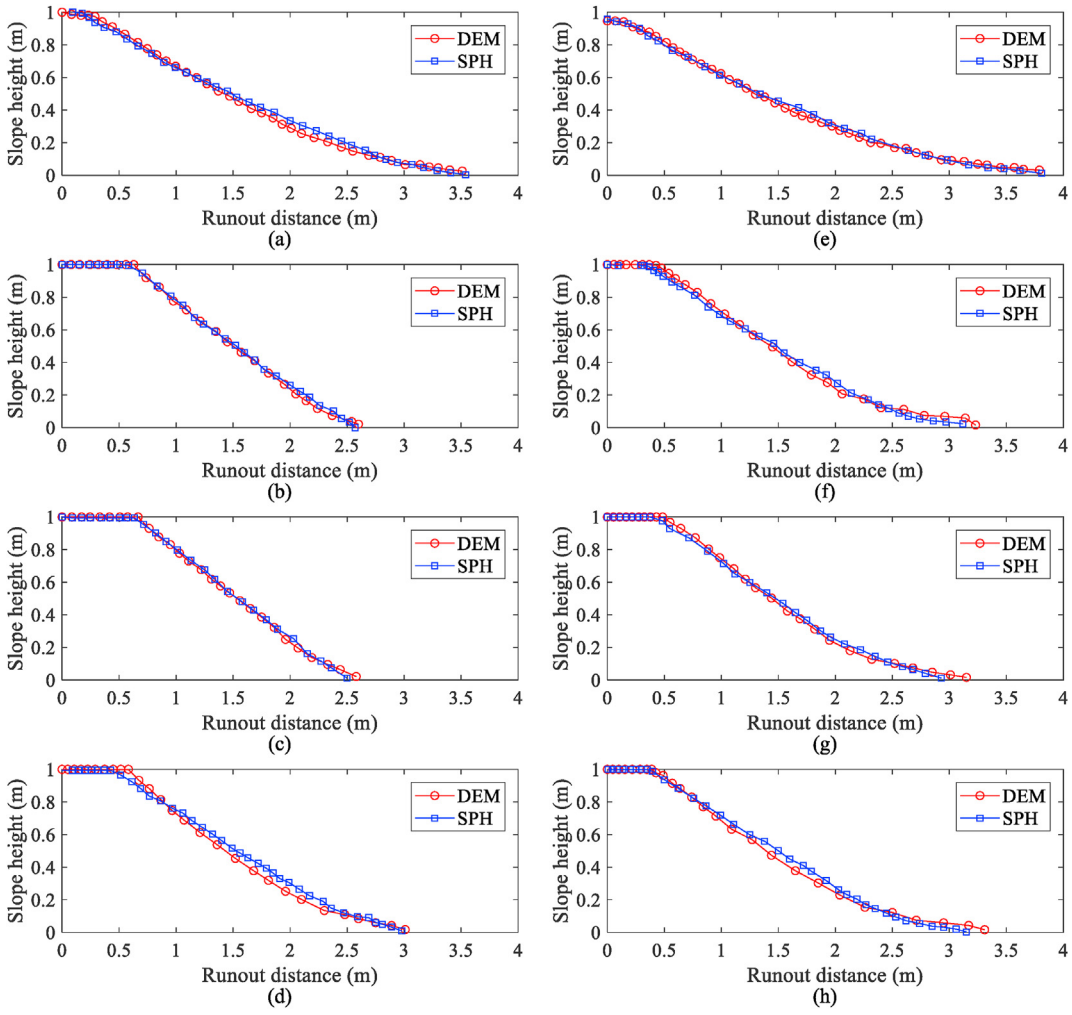

Fig. 8. Comparison of final deposit configurations using DEM and SPH: (a)–(d) "Dense" slopes with (a) SS (no rolling resistance), (b) TS, (c) ES, and (d) SS (rolling resistance of 0.1); (e)–(h) "Loose" slopes with (e) SS (no rolling resistance), (f) TS, (g) ES, and (h) SS (rolling resistance of 0.1).

the final stable state (compared with the SS cases where the rolling resistance is considered equal to zero).

The porosity distributions of slope collapse at the final stable state are finally provided in Fig. 10 (SPH simulations). It can be observed that the porosity in the non-sliding area remains basically unchanged (before and after the landslide), while it increases in the sliding area. This is due to the particle redistribution after the landslide. For the loose slopes, it is also worth noting that the porosity distribution of the sliding area does not tend to be looser and the porosity does not significantly change. One possible reason is that the spatial distribution of the particles after collapse is similar to that at the initial state. Another explanation could be that the shear expansion caused by the particles in the sliding area is not significant.

6. Conclusions

Based on the critical state sand model SIMSAND and the SPH method, a highly efficient and accurate approach for numerical simulation of slope collapse is proposed in this paper. Using DEM results as benchmark studies, a total of 8 slopes with different initial conditions were simulated: 3 different particle shapes (SS, TS and ES), and 2 different initial densities (dense and loose), and a set of numerical simulations considering the anti-rotation effect of spherical particles were studied. The results of landslide distance, particle rotation and velocity distribution were analyzed.

Comparisons show that the adopted numerical strategy is able to reproduce qualitatively and quantitatively the main characteristics of slope collapse, i.e. free surface, final deposit configurations and final runout distance. The results also illustrate that the particle shape, initial density and particle anti-rotation coefficient have a significant effect on the landslide. Compared with regular spherical particles, the slope generated by irregular particles is less prone to sliding damage, its sliding area is smaller and the impact of landslide damage is less. Particles with irregular shape can therefore restrict the rotation of the particles. Compared with the "loose" slope, the "dense" slope presents less landslide damage. The numerical simulation results of regular tetrahedral and elongated particles are similar, indicating that these two particle shapes have similar restraining effects on particle rotation.

The combination of SPH with the SIMSAND critical state constitutive model is able to reproduce slope collapse considering the effect of particle shapes and soil densities. The proposed

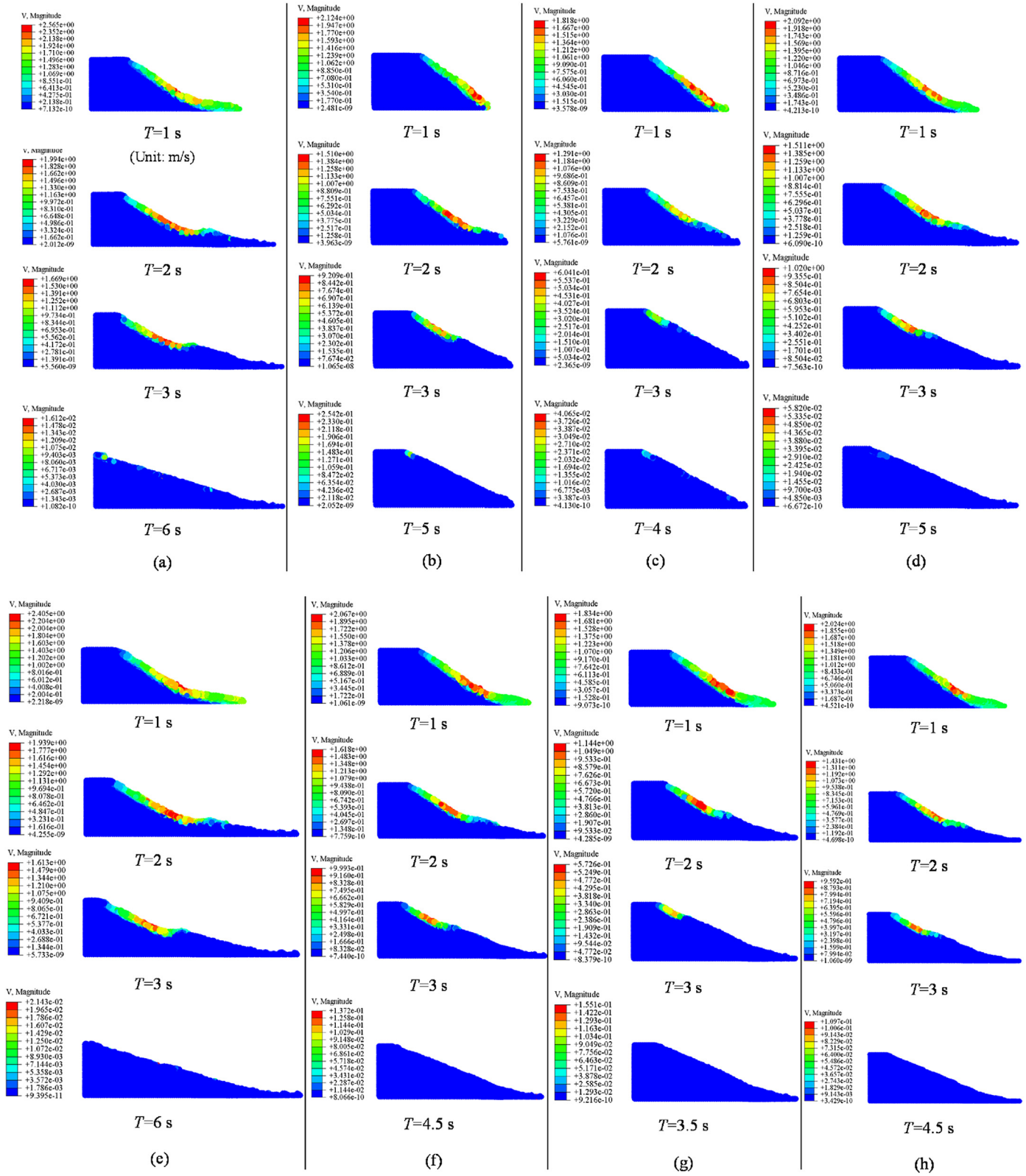

Fig. 9. Velocity field variation during collapse using SPH: (a)–(d) "Dense" slopes with (a) SS (no rolling resistance), (b) TS, (c) ES, and (d) SS (rolling resistance of 0.1); (e)–(h) "Loose" slopes with (e) SS (no rolling resistance), (f) TS, (g) ES, and (h) SS (rolling resistance of 0.1).

strategy has a higher computational efficiency compared to DEM, while maintaining the computational accuracy. Therefore, it is an effective numerical tool that can be further applied to study real scale field landslides.

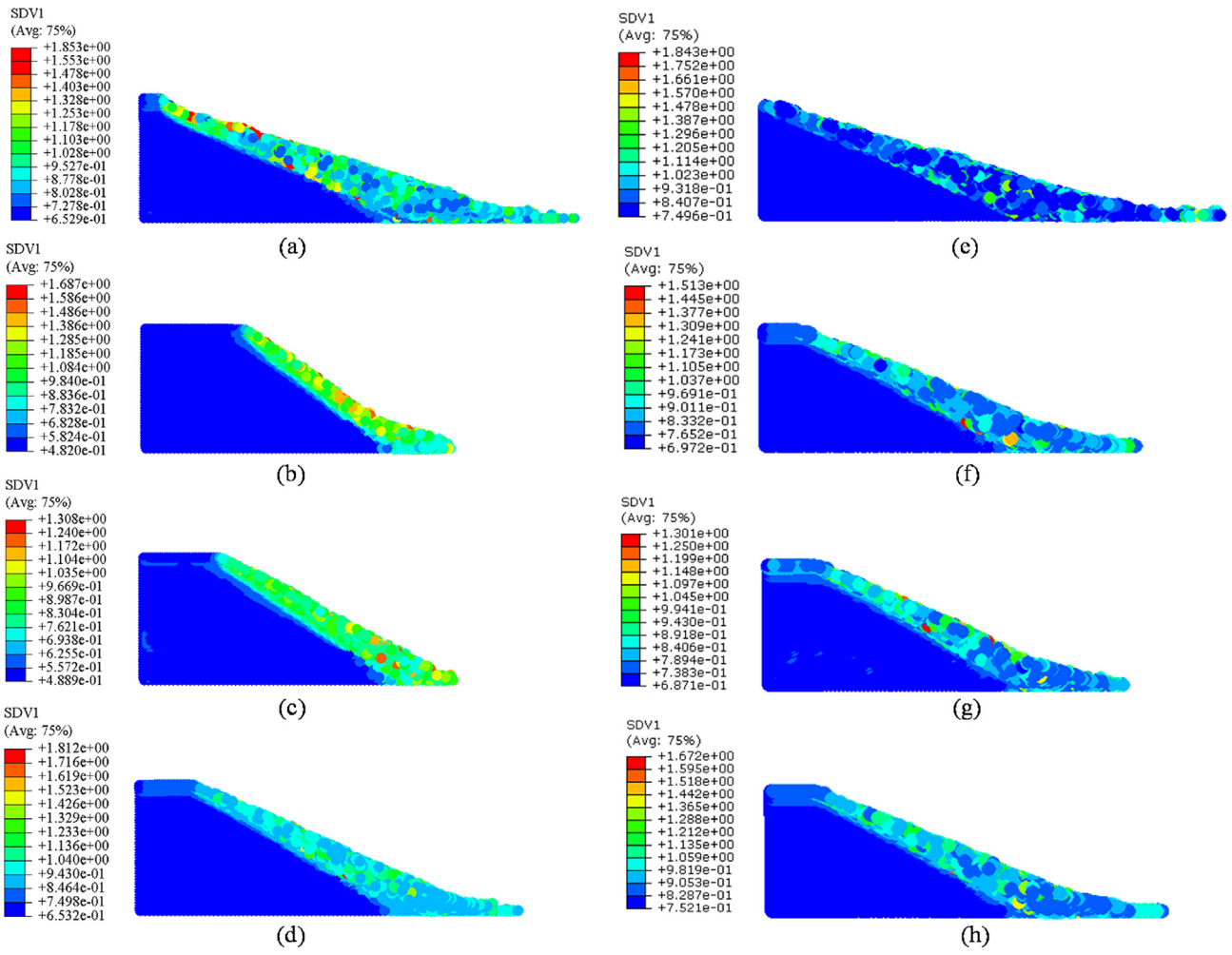

Fig. 10. Porosity distribution at the final state using SPH: (a)–(d) "Dense" slopes with (a) SS (no rolling resistance), (b) TS, (c) ES, and (d) SS (rolling resistance of 0.1); (e)–(h) "Loose" slopes with (e) SS (no rolling resistance), (f) TS, (g) ES, and (h) SS (rolling resistance of 0.1).

Declaration of competing interest

The authors declare that they have no known competing financial interests or personal relationships that could have appeared to influence the work reported in this paper.

Acknowledgments

This research is supported by Shenzhen (China) Science and Technology Innovation Committee (Grant Nos. JSGG2018 0504170449754), and the numerical simulations are supported by Center for Computational Science and Engineering at Southern University of Science and Technology, Shenzhen, China.

References

Baranowski, P., Janiszewski, J., Malachowski, J., 2014. Study on computational methods applied to modelling of pulse shaper in split-Hopkinson bar. Arch. Mech. 66 (6), 429–452.
Barla, M., Piovano, G., Grasselli, G., 2012. Rock slide simulation with the combined finite-discrete element method. Int. J. GeoMech. 12 (6), 711–721.
Bovet, E., Chiaia, B., Preziosi, L., 2010. A new model for snow avalanche dynamics based on non-Newtonian fluids. Meccanica 45 (6), 753–765.
Cascini, L., Cuomo, S., Pastor, M., Sorbino, G., Piciullo, L., 2014. SPH run-out modelling of channelised landslides of the flow type. Geomorphology 214, 502–513.
Coulomb, C.A., 1973. Essai sur une application des regles de maximis et minimis a quelques problemes de statique relatifs a l'architecture. Acad. R. Sci. Pairs France 343–382 (in French).
Di, Y., Sato, T., 2003. Liquefaction analysis of saturated soils taking into account variation in porosity and permeability with large deformation. Comput. Geotech. 30 (7), 623–635.
Gingold, R.A., Monaghan, J.J., 1977. Smoothed particle hydrodynamics: theory and application to non-spherical stars. Mon. Not. Roy. Astron. Soc. 181 (3), 375–389.
Haddad, B., Pastor, M., Palacios, D., Munoz-Salinas, E., 2010. A SPH depth integrated model for Popocatépetl 2001 lahar (Mexico): sensitivity analysis and runout simulation. Eng. Geol. 114 (3–4), 312–329.
Hibbitt, Karlsson, Sorensen Inc, 2014. ABAQUS/Explicit: User's Manual. Pawtucket, USA, Version 6.14.
Hong, Y., He, B., Wang, L.Z., Wang, Z., Ng, C.W.W., Mašín, D., 2017. Cyclic lateral response and failure mechanisms of semi-rigid pile in soft clay: centrifuge tests and numerical modelling. Can. Geotech. J. 54 (6), 806–824.
Hong, Y., Wang, L.Z., Zhang, J.F., Gao, Z.W., 2020. 3D elastoplastic model for fine-grained gassy soil considering the gas-dependent yield surface shape and stress-dilatancy. J. Eng. Mech. 146 (5), 04020037.
Jeong, S.S., Lee, K.W., Ko, J.Y., 2015. A study on the 3D analysis of debris flow based on large deformation technique (coupled Eulerian-Lagrangian). J. Korean Geotech. Soc. 31 (12), 45–57.
Jin, Y.F., Yin, Z.Y., Shen, S.L., Hicher, P.Y., 2016a. Investigation into MOGA for identifying parameters of a critical-state-based sand model and parameters correlation by factor analysis. Acta Geotech. 11 (5), 1131–1145.
Jin, Y.F., Yin, Z.Y., Shen, S.L., Hicher, P.Y., 2016b. Selection of sand models and identification of parameters using an enhanced genetic algorithm. Int. J. Numer. Anal. Methods GeoMech. 40, 1219–1240.
Jin, Y.F., Wu, Z.X., Yin, Z.Y., Shen, J.S., 2017a. Estimation of critical state-related formula in advanced constitutive modeling of granular material. Acta Geotech. (12), 1329–1351.

Jin, Y.F., Yin, Z.Y., Shen, S.L., Zhang, D.M., 2017b. A new hybrid real-coded genetic algorithm and its application to parameters identification of soils. Inverse Probl. Sci. Eng. 25 (9), 1343–1366.
Jin, Z., Yin, Z.Y., Kotronis, P., Jin, Y.F., 2018a. Numerical investigation on evolving failure of caisson foundation in sand using the combined Lagrangian-SPH method. Mar. Georesour. Geotechnol. 37 (1), 23–35.
Jin, Y.F., Yin, Z.Y., Wu, Z.X., Zhou, W.H., 2018b. Identifying parameters of easily crushable sand and application to offshore pile driving. Ocean. Eng. 154, 416–429.
Jin, Y.F., Yin, Z.Y., Zhou, W.H., Huang, H.W., 2019a. Multi-objective optimization-based updating of predictions during excavation. Eng. Appl. Artif. Intell. 78, 102–123.
Jin, Y.F., Yin, Z.Y., Zhou, W.H., Horpibulsuk, S., 2019b. Identifying parameters of advanced soil models using an enhanced transitional Markov chain Monte Carlo method. Acta Geotech. 14 (6), 1925–1947.
Jin, Y.F., Yin, Z.Y., 2020. Enhancement of backtracking search algorithm for identifying soil parameters. Int. J. Numer. Anal. Methods GeoMech. (44), 1239–1261.
Lacaze, L., Phillips, J.C., Kerswell, R.R., 2008. Planar collapse of a granular column: experiments and discrete element simulations. Phys. Fluids 20, 063302.
Lei, X.Q., He, S.M., Chen, X.Q., Wong, H.K.K., Wu, L.Z., Liu, E.L., 2020. A generalized interpolation material point method for modelling coupled seepage-erosion-deformation process within unsaturated soils. Adv. Water Resour. 103578. http://doi:10.1016/j.advwatres.2020.103578.
Liu, W.K., Jun, S., Li, S.F., Adee, J., Belytschko, T., 1995. Reproducing kernel particle methods for structural dynamics. Int. J. Numer. Methods Eng. 38 (10), 1655–1679.
Llano-Serna, M.A., Farias, M.M., Pedroso, D.M., 2016. An assessment of the material point method for modelling large scale run-out processes in landslides. Landslides 13 (5), 1057–1066.
Lu, C.Y., Tang, C.L., Chan, Y.C., Hu, J.C., Chi, C.C., 2014. Forecasting landslide hazard by the 3D discrete element method: a case study of the unstable slope in the Lushan hot spring district, central Taiwan. Eng. Geol. 183, 14–30.
Maeda, K., Sakai, H., Sakai, M., 2006. Development of seepage failure analysis method of ground with smoothed particle hydrodynamics. Struct. Eng./Earthq. Eng. 23 (2), 307s–319s.
McDougall, S., Hungr, O., 2004. A model for the analysis of rapid landslide motion across three-dimensional terrain. Can. Geotech. J. 41 (6), 1084–1097.
Ortiz, M., Simo, J., 1986. An analysis of a new class of integration algorithms for elastoplastic constitutive relations. Int. J. Numer. Methods Eng. 23 (3), 353–366.
Peng, C., Wang, S., Wu, W., Yu, H.-s., Wang, C., Chen, J.Y., 2019. LOQUAT: an open-source GPU-accelerated SPH solver for geotechnical modeling. Acta Geotech. 14 (5), 1269–1287.
Ren, H.L., Zhuang, X.Y., Rabczuk, T., Chester, R., 2019. A dual-support smoothed particle hydrodynamics for weakly compressible fluid inspired by the dual-horizon peridynamics. Comput. Model. Eng. Sci. 121 (2), 353–383.
Roscoe, K.H., Burland, J.B., 1968. In: Heyman, J., Leckie, F.A. (Eds.), On the Generalized Stress-Strain Behaviour of Wet Clay. Engineeringplasticity Cambridge University Press, Cambridge, UK, pp. 535–609.
Scholtès, L., Donzé, F.V., 2012. Modelling progressive failure in fractured rock masses using a 3D discrete element method. Int. J. Rock Mech. Min. Sci. 52, 18–30.
Shakibaeinia, A., Jin, Y.C., 2011. A mesh-free particle model for simulation of mobile-bed dam break. Adv. Water Resour. 34 (6), 794–807.
Sheng, D.C., Sloan, S.W., Yu, H.S., 2000. Aspects of finite element implementation of critical state models. Comput. Mech. 26 (2), 185–196.
Shi, J.W., Fu, Z.Z., Guo, W.L., 2019. Investigation of geometric effects on three-dimensional tunnel deformation mechanisms due to basement excavation. Comput. Geotech. 106, 108–116.
Soga, K., Alonso, E., Yerro, A., Kumar, K., Bandara, S., 2016. Trends in large-deformation analysis of landslide mass movements with particular emphasis on the material point method. Geotechnique 66 (3), 248–273.
Soundararajan, K.K., 2015. Multi-scale Multiphase Modelling of Granular Flows. PhD Thesis. University of Cambridge, Cambridge, UK.
Utili, S., Zhao, T., Houlsby, G.T., 2015. 3D DEM investigation of granular column collapse: evaluation of debris motion and its destructive power. Eng. Geol. 186, 3–16.
Wang, J.G., Wang, S., Su, A.J., Xiang, W., Xiong, C.R., Blum, P., 2021. Simulating landslide-induced tsunamis in the Yangtze river at the three Gorges in China. Acta Geotech. 1–17.
Wu, Z.X., Yin, Z.Y., Jin, Y.F., Geng, X.Y., 2017. A straightforward procedure of parameters determination for sand: a bridge from critical state based constitutive modelling to finite element analysis. Eur. J. Environ. Civil Eng. 23 (12), 1–23.
Xiong, H., Yin, Z.Y., Nicot, F., Wautier, A., Marie, M., Darve, F., Veylon, G., Philippe, P., 2021. A novel multi-scale large deformation approach for modelling of granular collapse. Acta Geotech. https://doi.org/10.1007/s11440-020-01113-5.
Yang, J., Yin, Z.Y., Laouafa, F., Hicher, P.Y., 2019a. Internal erosion in dike-on-foundation modeled by a coupled hydromechanical approach. Int. J. Numer. Anal. Methods GeoMech. 43 (3), 663–683.
Yang, J., Yin, Z.Y., Laouafa, F., Hicher, P.Y., 2019b. Modeling coupled erosion and filtration of fine particles in granular media. Acta Geotech. 14 (6), 1615–1627.
Yang, J., Yin, Z.Y., Laouafa, F., Hicher, P.Y., 2020. Hydromechanical modeling of granular soils considering internal erosion. Can. Geotech. J. 57 (2), 157–172.
Yao, Y.P., Lu, D.C., Zhou, A.N., Zou, B., 2004. Generalized non-linear strength theory and transformed stress space. Sci. China E 47 (6), 691–709.
Yao, Y.P., Sun, D.A., Matsuoka, H., 2008. A unified constitutive model for both clay and sand with hardening parameter independent on stress path. Comput. Geotech. 35 (2), 210–222.
Yao, Y.P., Hou, W., Zhou, A.N., 2009. UH model: three-dimensional unified hardening model for overconsolidated clays. Geotechnique 59 (5), 451–469.
Yin, Z.Y., Chang, C.S., Hicher, P.Y., 2010. Micromechanical modelling for effect of inherent anisotropy on cyclic behaviour of sand. Int. J. Solid Struct. 47 (14–15), 1933–1951.
Yin, Z.Y., Chang, C.S., 2013. Stress–dilatancy behavior for sand under loading and unloading conditions. Int. J. Numer. Anal. Methods GeoMech. 37 (8), 855–870.
Yin, Z.Y., Hicher, P.Y., Dano, C., Jin, Y.F., 2016. Modeling mechanical behavior of very coarse granular materials. J. Eng. Mech. 143 (1), C4016006.
Yin, Z.Y., Jin, Y.F., Shen, S.L., Huang, H.W., 2017. An efficient optimization method for identifying parameters of soft structured clay by an enhanced genetic algorithm and elastic–viscoplastic model. Acta Geotech. 12 (4), 849–867.
Yin, Z.Y., Jin, Z., Kotronis, P., Wu, Z.X., 2018a. Novel SPH SIMSAND–based approach for modeling of granular collapse. Int. J. GeoMech. 18 (11), 04018156.
Yin, Z.Y., Jin, Y.F., Shen, J.S., Hicher, P.Y., 2018b. Optimization techniques for identifying soil parameters in geotechnical engineering: comparative study and enhancement. Int. J. Numer. Anal. Methods GeoMech. 42 (1), 70–94.

Dr. Zhuang Jin received his PhD degree at Ecole Centrale de Nantes, France in 2019 and then works as a post-doctor at the Department of Ocean Science and Engineering of Southern University of Science and Technology, China. His research interests involve large deformation issues in geotechnical engineering and soil-structure interaction (SSI) for mooring foundations in ocean engineering. Up to now, he has published nearly 10 technical papers.